UNCERTAINTY IN PROPELLANT FIRE HEAT FLUX—AN EXPERIMENTAL AND MODELING APPROACH

William W. Erikson, ,Vernon F. Nicolette, Walter Gill, and Sheldon R. Tieszen
Sandia National Laboratories*
Albuquerque, NM 87185-0836

ABSTRACT

Solid propellant fires produce severe thermal environments. The radiant heat flux produced by these fires is an important quantity in determining safe working ranges and hazard zones for storage facilities as well as in assessing the potential for sympathetic (fratricidal) ignition of munitions. But because heat flux is an indirectly measured quantity, it is often fraught with large levels of uncertainty. This in turn introduces large uncertainties into the predicted response of items of interest, which ultimately adversely impacts outcomes of safety studies.

At Sandia National Laboratories, we address this issue by using a combined experimental and modeling approach for determining the heat flux from solid propellant fires. Our approach allows propagating the heat flux uncertainty from the original heat flux determination through to the modeling in the safety studies. By introducing modeling up front in the process we also have some degree of control over the level of uncertainty. In this paper, we introduce these notions in an example case.

In experiments conducted at SNL in 2007, cylinders of solid propellant were burned in a controlled, indoor environment. The experimental apparatus was specifically designed to facilitate comparison between model and experiment, in keeping with our longstanding philosophy: “test what you can model; model what you can test.” Measurements of radiant heat flux were made with three different types of commercial and specialty gages—each with its own set of associated limitations and uncertainty quantities. A thorough study of the uncertainty of the specialty gauges has been performed using detailed thermal modeling of the response of the gauges to a nearby propellant fire. As part of the modeling, it is also necessary to consider the environment as well. To meet this need, we rely on fire simulation codes to assess thermal behavior of propellant fire plumes and objects exposed to those fires. The codes include physics-based models to represent the observed complex behavior. Significant progress has been made toward a predictive capability. However, model limitations (physics model approximations, discretization errors, uncertain inputs, inherent stochastics, etc.) result in some level of uncertainty in the simulations as well. In our process, we compare of heat flux gauge experimental responses in an actual fire to heat fluxes predicted from computational code in light of the uncertainties. This allows the validation of the code with accompanying error bars for use in the safety studies.

INTRODUCTION

Solid rocket propellants are designed to burn at elevated pressure inside a rocket chamber at specific design conditions, but they will burn at ambient pressures as well. Heat transfer from ambient pressure combustion of solid propellants is important in many different scenarios—accidental or otherwise. Combustion temperatures and heat fluxes are sufficiently high that they can: (1) quickly ignite adjacent material leading to substantial loss of life and equipment (e.g. USS Stark incident[1]); (2) lead to ignition or explosion of other nearby devices (warheads, munitions, other rocket motors) in transportation or storage incidents; (3) vaporize radioisotopic fuels used in deep-space probes (relevant to launch safety analyses) and (4) dictate the quantities and methods required for safely disposing of surplus material in demilitarization processes.

In the past, our efforts on understanding heat transfer from ambient-air propellant have focused on objects subjected to direct impingement by the propellant combustion products[2,3]. To be sure, direct impingement does result in the most severe thermal load; however, heat transfer to external objects is also of interest for safety analysis purposes. While in-plume objects are subjected to a combined thermal environment, including convection, radiation, and material deposition, the heat transfer to external objects is essentially due to the mechanism of thermal radiation alone.

It should be noted that radiation heat transfer is based on exchanges. It is not only a function of the source (i.e. the fire) which radiates to the object but also the object itself which radiates back to the fire. An object which

* Sandia is a multiprogram laboratory operated by Sandia Corporation, a Lockheed Martin Company, for the United States Department of Energy’s National Nuclear Security Administration under contract DE-AC04-94AL85000.

heats up very quickly will be subjected to a different net radiative heat flux history than a more thermally massive object which heats up more slowly. Surface properties such as emissivity, absorptivity, and reflectivity also play a role in the net radiative heat transfer to an object. In order to make results transferable from one scenario to another and facilitate scaling relationships (distance, fire size, etc.) we would like results to be independent of the object response. Radiation intensity, I, (having units of energy flux per unit area per unit solid angle, W/m^2-sr) is one such quantity; another is the hemispherically integrated intensity or incident radiant heat flux, q_{inc} (also known as "cold wall flux, having units of W/m^2). Intensity should be independent of distance from a source whereas incident radiant flux depends on the distance from the source (inversely proportional to distance squared for a point radiation source).

A variety of sensors can be devised to measure radiant energy. Some capture photons and convert to electrical signals which can be converted to energy flux levels. Many practical sensors consist of an object designed to absorb energy and a method of measuring temperature and temperature gradients within the object (typically by means of thermocouples or thermopiles). Gardon gauges and Schmitt-Boelter gauges are examples of commercially available devices well-suited for measuring radiant heat fluxes external to fires. However these gauges are fraught with a number of issues (fouling, sooting, failure) when used within flames. To circumvent these problems, researchers have devised additional devices which are rugged enough to be deployed within fires. Two of these are known as the Sandia Heat Flux Gauge (SHFG)[4] and the Directional Flame Thermometer (DFT)[5,6]. Diagrams of the two devices are shown in Figs. 1 and 2. Each of them was designed with two sensor faces—exposure in two opposite directions can be measured at once.

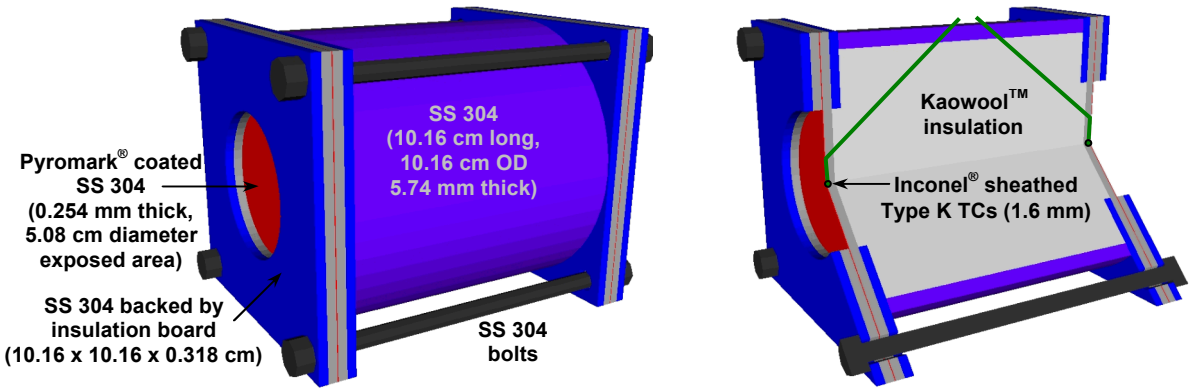

Fig. 1: Diagram of Sandia Heat Flux Gauge (SHFG) with cutaway.

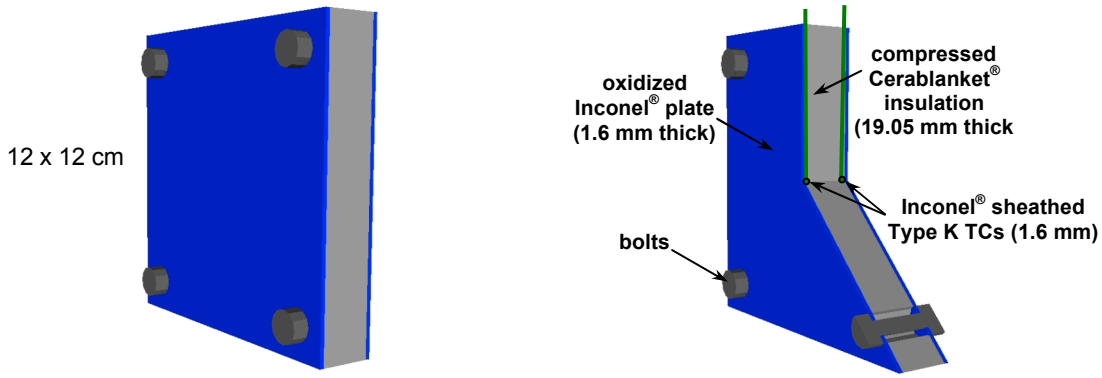

Fig. 2: Diagram of Directional Flame Thermometer (DFT) with cutaway.

While the SHFG and the DFT were primarily designed for use within fires, they have been deployed on the exterior of fires as well. One drawback of each of these is that the temperatures measured must be interpreted and converted to yield the incident heat flux. Numerical algorithms have been developed for each which allows incident heat flux to be obtained. Properties (thermal conductivity, heat capacity, emissivity) of the constituent materials are required as part of the flux interpretation processes and uncertainties in these properties are manifest as uncertainties or error bars in the derived incident heat flux. Geometry also plays a role in that often the time-

temperature histories are converted to heat assuming the heat transfer is locally one-dimensional. Departures from this assumption also contribute to the error bars.

In this work we have used finite element models of the SHFG and DFT in order to help assess the uncertainty in incident flux measurements made using these devices. We use the derived uncertainties to build confidence intervals around measurements from recent ambient air solid propellant burn tests. We also compare with computational fluid dynamics (CFD) simulation results.

FINITE ELEMENT MODELS OF GAUGES

Idealized behavior of the two gauges can be captured by fairly simple, even one-dimensional models. However, in order to assess uncertainties of the actual hardware, it is necessary to faithfully reproduce the actual structure as well as possible. For instance, documents describing both the SHFG and DFT describe time lags associated with the thermocouples attached to the sensor plates. Also there is potential for multi-dimensional heat transfer (such as down the connecting bolts) which can lead to uncertainties which cannot be captured by simple models. Hence, we have included sufficient detail to capture much of the non-ideal real world behavior.

Figures 3 and 4 show the finite element meshes used. The models included several layers of elements through the sensor plates to adequately capture large temperature gradients which are expected under high-heat flux conditions. For accuracy through thin layers, a hexahedral mesh was used throughout with the exception of the Inconel® sheathed thermocouples. These were modeled using bar finite elements having properties of Inconel®. They were tied to the rest of the structure using additional bar elements which provided contact resistance elements tuned to reproduce the temperature time lags observed in the real hardware (reported as 5.36 seconds from temperature ramp tests for the SHFG[4] and 1.9 seconds from step temperature response for the DFT[5]).

As part of the finite element models, containment structures were built to surround the ends and sides of each gauge with separate full cavity enclosures. These structures were decoupled from the gauge mesh for thermal conduction, but are allowed to radiate to exposed surface. By means of these, full hemispherical blackbody radiative boundary conditions were applied to provide known inputs for comparison purposes.

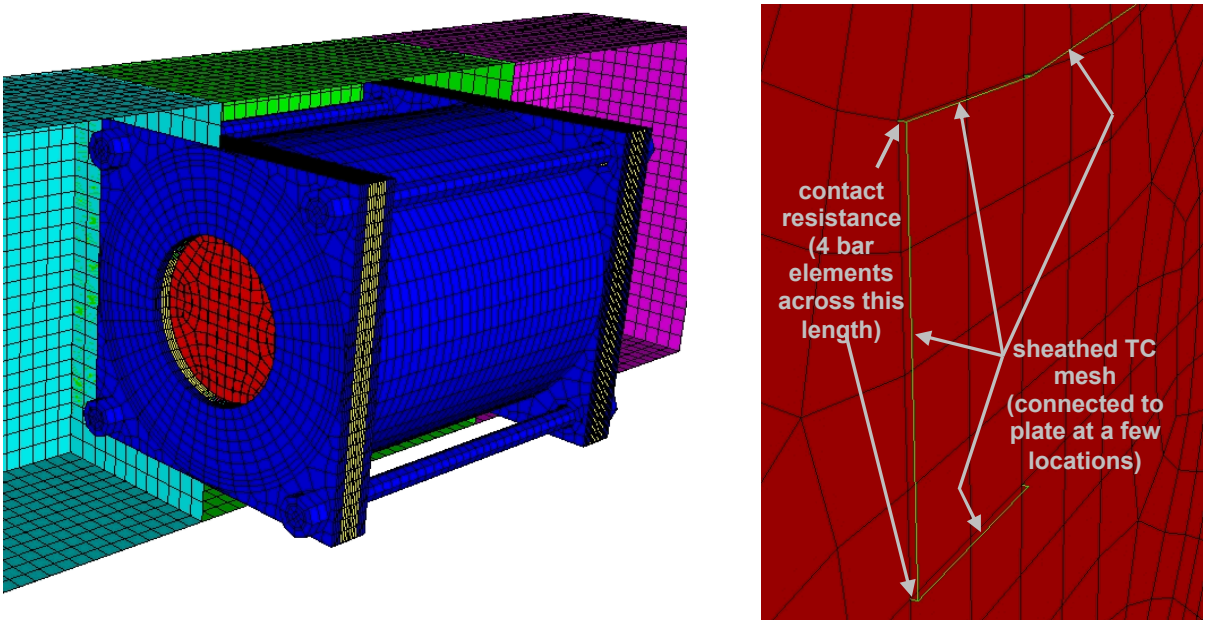

Fig. 3: Finite element mesh of SHFG. Left: device mesh within radiation enclosures (3, shown as cutaways) used for applying known boundary conditions to the various sections. Right: detail of sensor plate mesh showing bar elements used to represent sheathed thermocouple and connect it to plate. The thermocouple was mounted to the plate in a 'C' shape. The bar elements shown in the figure are not to scale—in reality the thermocouple sheathing is thicker (1.6 mm) than the sensor plate (0.254 mm). The properties of the bar elements used in the model reflect the actual TC size.

Several test cases were devised to examine the behavior of the heat flux gauges. In each of these, the time-temperature histories of the thermocouple locations were obtained using results from the finite element heat

transfer code, CALORE. These temperature histories were then used to derive the incident heat flux using the appropriate sets of processing software. For the SHFG, a spreadsheet macro which assumes one-dimensional heat flow has been developed for processing data.[4] For the DFT, a commercial inverse heat conduction code, IHCP1D[7], was used to obtain net heat flux and temperature at the surface of the sensor plate (opposite side from the TC); these results were then used to back out the incident heat flux by appealing to a surface energy balance. In Eq. 1, q_{net} is the net heat flux, q_{inc} is the incident heat flux, α is the absorptivity (so αq_{inc} is the absorbed heat flux), ε is the emissivity, σ is the Stefan-Boltzmann constant, and T_s is the surface temperature (so $\varepsilon\sigma T_s^4$ represents the emitted heat flux).

$$q_{net} = \alpha q_{inc} - \varepsilon\sigma T_s^4 \qquad (1)$$

If we make the usual assumption that $\alpha=\varepsilon$ (Kirchoff's identity) then we can solve for q_{inc} in terms of q_{net} and T_s:

$$q_{inc} = q_{net} / \alpha + \sigma T_s^4 \qquad (2)$$

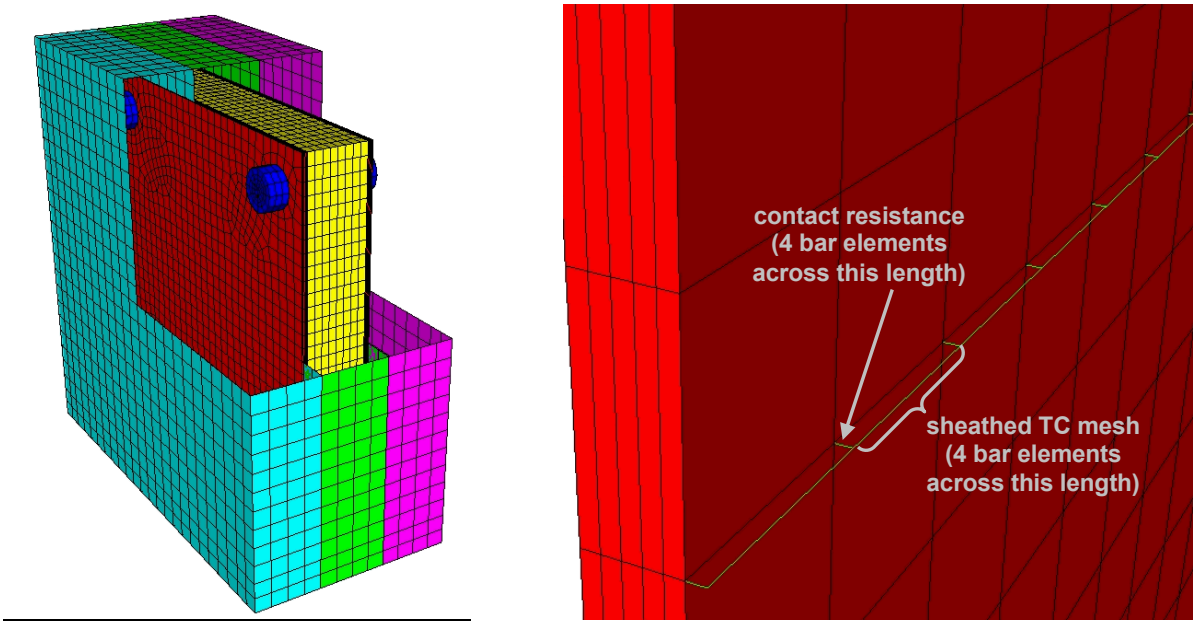

Fig. 4: Finite element mesh of DFT. Left: device mesh within radiation enclosures (3, shown as cutaways) used for applying known boundary conditions to the various sections. Right: detail of sensor plate mesh showing bar elements used to represent sheathed thermocouple and connect it to plate.

The first baseline case consisted of a ramp-and-hold temperature profile up to 900 K (blackbody, ε=1) applied on one end with a 300 K blackbody condition applied on the other end and on the sides. The 100 second length of time for the full exposure boundary condition application corresponds nominally with recent propellant fire experiments conducted at Sandia National Laboratories. Figure 5 shows the temperature and incident radiant heat flux associated with this baseline case.

Other test cases mimicked the time-temperature ramp-and-hold profile of the Case 1 with a few variations. Case 2 was the same as Case 1, but the side enclosure followed a ramp-and-hold profile to 650 K. Case 3 was applied to the SHFG but not the DFT; it was identical to Case 1 but the emissivity of all SHFG surfaces was set to 0.0 such that only the exposed sensor face was absorbing heat. Case 4 applied the same 900 K ramp-and-hold boundary condition on the back and side enclosures as well as on the front. In the other cases, only the front side had the ramp-and-hold profile, but the hold temperature was changed to: 500 K (Case 5), 700 K (Case 6), 1100 K (Case 7), or 1300 K (Case 8).

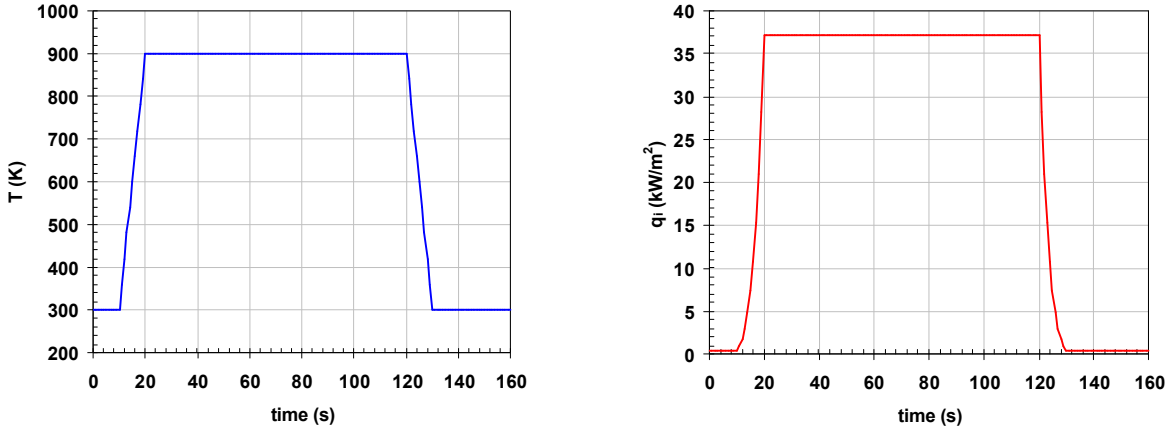

Fig. 5: Boundary conditions applied in Baseline Test Case 1. Left: Temperature; Right, incident radiant heat flux.

Figure 6 shows the results of Cases 1 to 8 compared with the known incident radiant heat flux (σT^4). Note that the DFT gauges had significantly better response than the SHFG. If we ignore the initial transients (associated with the thermocouple time lag) and only consider times between 30 and 120, the DFT result is within ± 5% of the actual value, whereas the SHFG results under-predicts the results by between 20 to 43%.

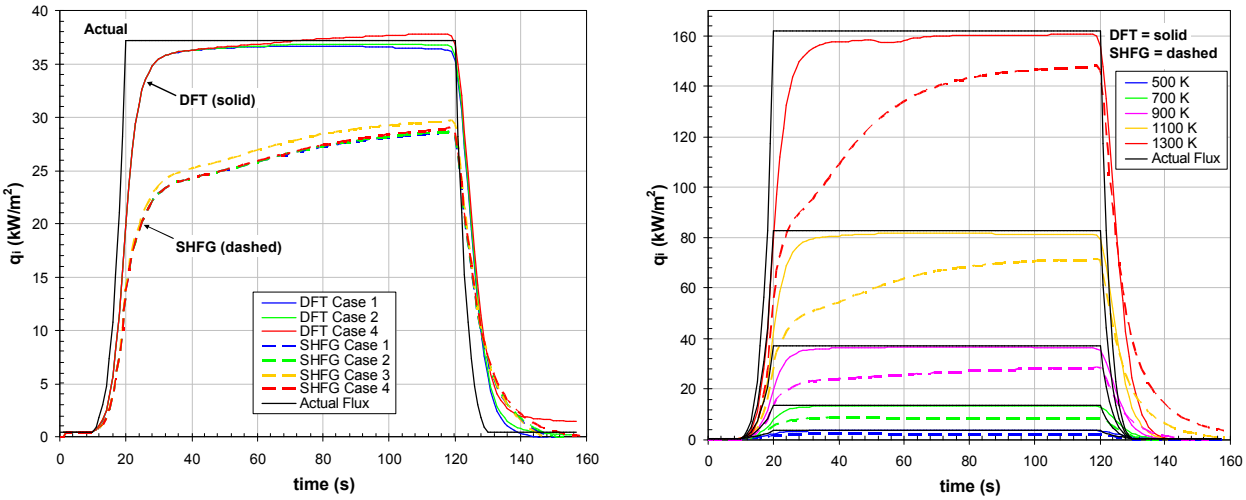

Fig. 6: Derived incident heat flux for baseline test cases. Left: Cases 1 to 4 (variations at 900 K); Right: Cases 1, 5, 6, 7, 8 (variations of hold temperature).

It is believed that there are two main sources for the poor performance of the SHFG: first, because the sensor face is recessed, the exposed circle does not completely "see" the encompassing blackbody cavity. To check this effect, Case 3 was run in which all the emissivity of the external faces (except the circular sensor face) of the SHFG was set to 0. This made the making those surfaces perfectly reflective and allowed the circular face to "see" only the surrounding cavity. The effect was a small increase (~4%) in derived incident flux as shown in the left hand graph of Fig. 6.

The second and more important effect appears to be multi-dimensional heat losses within the thin sensor plate. Figure 7 shows the sensor plate temperature at a point 100 seconds into the Case 1 simulation for both the SHFG (left side) and the DFT (right side). In each figure the scale has been adjusted to show the minimum-to-maximum range of temperatures on each sensor plate. Note that the SHFG has a 480 K range due primarily to a large portion of the plate being unexposed to the incident radiation. The overall gradients in the vicinity of the thermocouple sensor are quite large leading to substantial lateral heat transfer in spite of the thin plate thickness. In contrast, the DFT has a temperature range of only 118 K; the primary cause of this is conductive losses through the bolts. Overall the temperature gradients in the vicinity of the thermocouple are small and the losses through the bolts, while present, seem to be less important. Interestingly, although no effort was made to thermally isolate the

bolts in the DFT design—there is pure metal-to-metal contact—the effect does seem to be minor over the time scales we have considered here.

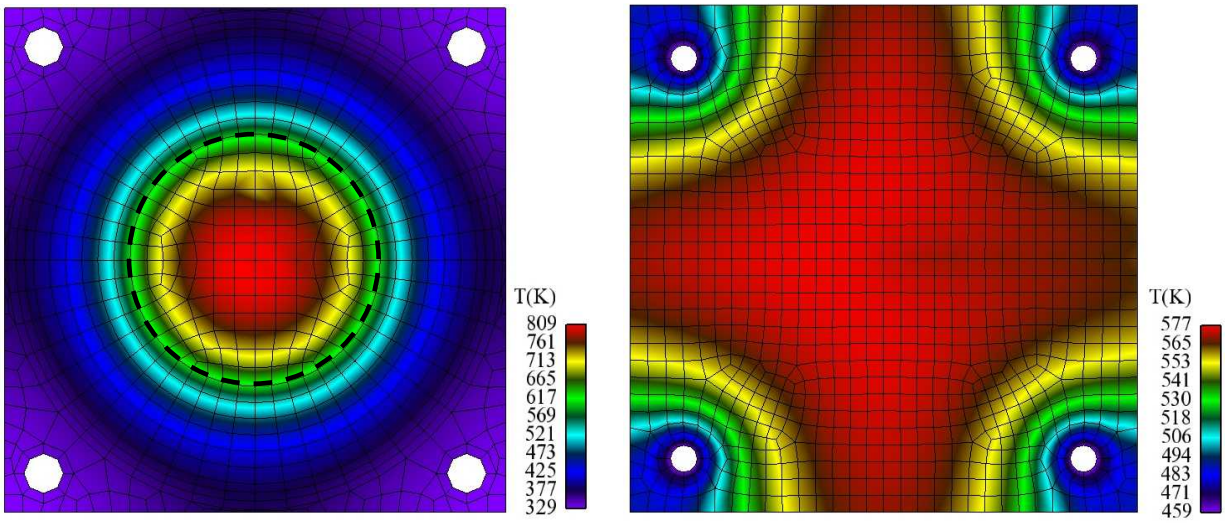

Fig. 7: Sensor plate temperatures at a simulation time of 100 s from Case 1. Left: SHFG; Right: DFT. Temperature ranges are adjusted to show a full minimum-to-maximum range for each. The dashed line in the SHFG image shows the location of the exposed region. Note the slight asymmetries caused by the thermocouple attachments in the models.

In order to check the effect of lateral heat losses in the SHFG sensor plate, temperature gradients at the sensor were obtained at the boundary of the sensor exposed area from the finite element simulations. These were used to calculate lateral heat losses as a function of time for the various test Cases from exposure temperatures of 500 K to 1300 K. The left hand side of Fig. 8 shows the lateral heat losses as a fraction of incident heat flux (i.e. the lateral losses [W] divided by the exposed area of the circle [m^2] normalized by the maximum incident heat flux). This equates to 10 to 33% of the incident radiant heat flux—a significant portion of the observed error in Fig. 6.

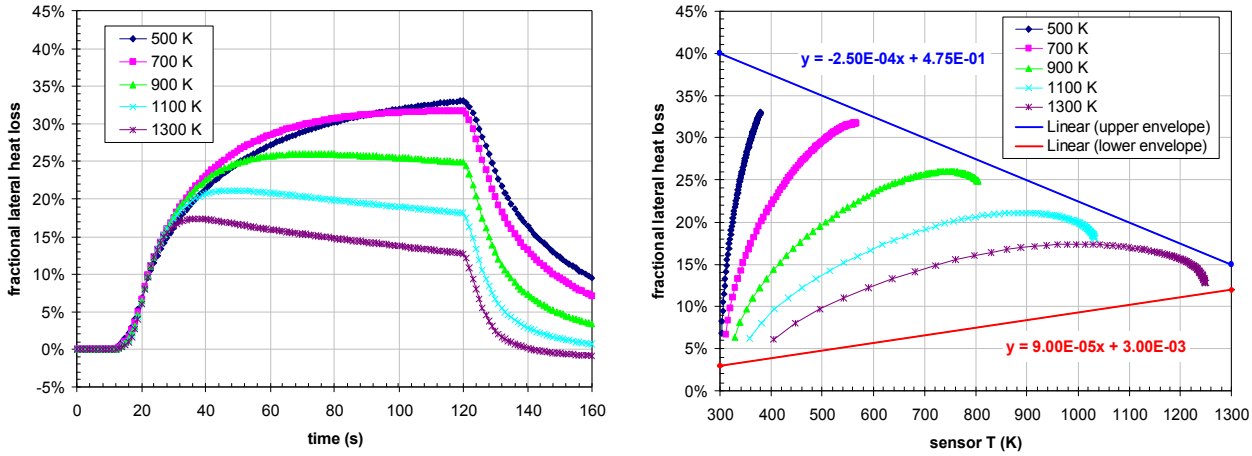

Fig. 8: Fractional energy loss from the SHFG as calculated from finite element solutions for Cases 1, 5, 6, 7, and 8. Left: plotted as a function of time; Right: plotted as a function of sensor temperature between times of 20 and 120 seconds. Straight lines form "envelopes" to capture the expected range of error.

Clearly it is necessary to account for the lateral heat losses in the SHFG to get a reasonable interpretation of experimental data. An attempt was made to correlate the lateral losses with the one piece of known data: the sensor temperature. The right hand side image of Fig. 8 shows the lateral heat losses plotted against the simulated thermocouple temperature between times of 20 and 120 seconds (when the incident flux was a constant maximum value). While it is clear that the heat losses are not a simple function of the sensor temperature, it appears that an "envelope" (upper and lower bounds) can be drawn around the data. This envelope could be used to give an

approximation to the lateral heat loss contribution to uncertainty bounds for results derived from actual experiments. This multi-dimensional uncertainty would be included along with the uncertainty bounds computed from the spreadsheet macro which only includes one-dimensional effects.

EXPERIMENTS

A series of open-air solid propellant combustion tests was conducted at Sandia National Laboratories in 2007 using an aluminized solid propellant. These tests were conducted in a large indoor facility in which the air flow was closely controlled. Four tests from that series will be considered here. These were upward-facing burns of cylindrical propellant samples of 15.2, 30.5, 45.7 and 50.8 cm (6, 12, 18 and 20") diameter. Each of these samples were 10.2 cm (4") thick and burned on the order of 100 seconds. A number of experimental diagnostics were employed on these tests including rod and plate calorimeters, scanning spectrometers, particle samplers, and external heat flux gauges. Several papers describing this test series and many of the diagnostics have been presented elsewhere.[8,9,10,11,12] Of interest here are the external heat flux gauges. Figure 9 shows the placement of the SHFGs, DFTs and Schmidt-Boelter (SB) gauges fielded on these tests. The SHFGs and DFTs were all fielded in coincident locations. Five of each were placed on a tower 1.54 m from the center of the charge; two others were placed in the corner of the facility. Both narrow angle and hemispherical SB gauges were fielded in these tests—one of each in two corners of the facility.

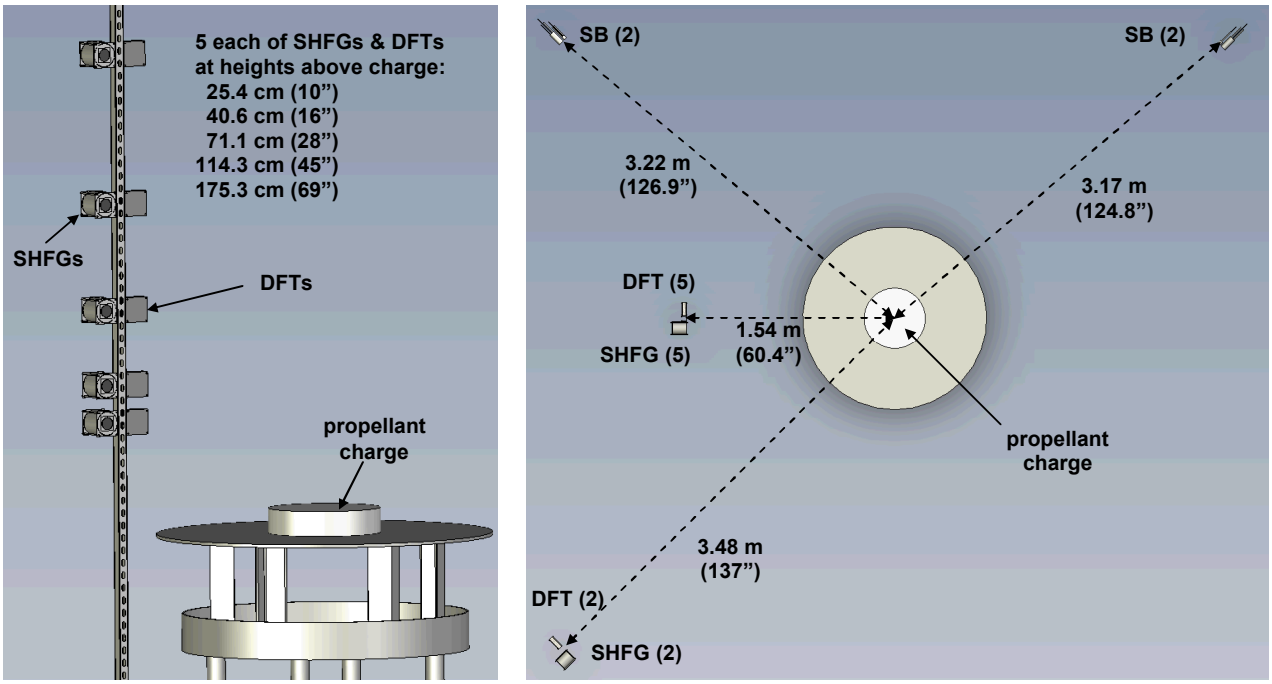

Fig. 9: Diagram showing location of external heat flux gauges fielded in propellant fire experiments. A total of 18 heat flux sensing devices were fielded (7 SHFGs, 7 DFTs, 2 narrow angle SB gauges and 2 hemispherical SB gauges). Left side shows elevation view looking toward the west side of the facility. Right side shows plan view.

EXPERIMENTAL UNCERTAINTY

Uncertainty in the DFT

As described previously, the analysis technique for the DFT involves using the IHCP1D inverse code. That code requires as inputs the material properties (heat capacity and conductivity) of the Inconel (C_1 and k_1) and Cerablanket® insulation (C_2 and k_2); as well as the material thicknesses for each layer (L_1 & L_2). The surface emissivity (ε) is not needed by IHCP1D, but it is required to obtain the incident heat flux via Eq. (2), so it is included as well. Sensitivity coefficients, σ, for each of these 7 parameters (C_1, C_2, k_1, k_2, L_1, L_2, and ε)—essentially numerical derivatives—were computed by a three step process. First, each of the parameters was perturbed one at a time

above and below the baseline value and IHCP1D was run at each condition. Second, Eq.(2) was used to process the results to yield q_{inc} for each combination of parameters. Finally, the numerical derivative for each parameter, was computed. Equation 3 shows an example of the numerical derivative with respect to C_1 where overbars represent the baseline value and δ is a perturbation. The others derivatives are computed in a similar fashion.

$$\sigma_{C_1} = \frac{\partial q_{inc}}{\partial C_1} = \frac{q_{inc}\left(\overline{C}_1 + \delta C_1, \overline{C}_2, \overline{k}_1, \overline{k}_2, \overline{L}_1, \overline{L}_2, \overline{\varepsilon}\right) - q_{inc}\left(\overline{C}_1 - \delta C_1, \overline{C}_2, \overline{k}_1, \overline{k}_2, \overline{L}_1, \overline{L}_2, \overline{\varepsilon}\right)}{2\delta C_1} \tag{3}$$

Once the sensitivity coefficients were obtained, they were multiplied by the expected uncertainty of each parameter (U_ϕ, representing uncertainty for parameter ϕ). The results were combined using a root-sum-of-squares approach as in Eq. 4 to yield the overall uncertainty in the incident heat flux.

$$U_{q_{inc}} = \sqrt{\left(\sigma_{C_1} U_{C_1}\right)^2 + \left(\sigma_{C_2} U_{C_2}\right)^2 + \left(\sigma_{k_1} U_{k_1}\right)^2 + \left(\sigma_{k_2} U_{k_2}\right)^2 + \left(\sigma_{L_1} U_{L_1}\right)^2 + \left(\sigma_{L_2} U_{L_2}\right)^2 + \left(\sigma_\varepsilon U_\varepsilon\right)^2} \tag{4}$$

One other useful piece of information is the "importance factor." In essence, importance factors, F_ϕ are the normalized fractional contributions of each of the uncertain parameters which show the relative contribution to the overall uncertainty. In mathematical form they are defined as in Eq. 5 (shown for parameter C_1, for example).

$$F_{C_1} = \frac{\left(\sigma_{C_1} U_{C_1}\right)^2}{\left(U_{q_{inc}}\right)^2} \tag{5}$$

The baseline properties used in the DFT analysis were based on those reported in Refs. 5 and 6. Uncertainties were estimated based on in Ref. 5 and engineering judgment. For instance, we expect heat capacity to be a quite well-known property for many materials, whereas conductivity is more difficult to measure and has a higher level of uncertainty. Furthermore, it is often more difficult to measure properties of materials like Cerablanket® and the estimated uncertainties reflect that. Table I lists the values of U_ϕ, used in the analysis here. Using the above outlined approach, incident heat flux and the associated uncertainties were calculated from the solid propellant tests.

Table I: Uncertain parameter values used in analysis of DFT

Parameter	Symbol	Nominal Value	Uncertainty Symbol	Value (fraction of nominal)
Inconel® heat capacity	$(\rho C_P)_1$	3,760,680* (J/m^3)	U_{C_1}	0.05
Cerablanket® heat capacity	$(\rho C_P)_2$	145,749* (J/m^3)	U_{C_2}	0.05
Inconel® conductivity	k_1	14.9* (W/m-K)	U_{k_1}	0.10
Cerablanket® conductivity	k_2	0.033* (W/m-K)	U_{k_2}	0.20
Inconel® thickness	L_1	0.16 cm	U_{L_1}	0.02
Cerablanket® thickness	L_2	1.905 cm	U_{L_2}	0.05
Inconel® emissivity	ε	0.77 ± 0.08**	U_ε	0.10

* Property is a function of temperature; room temperature value is shown.

** The emissivity has been reported using estimates ranging from 0.69 to 0.85. Here we use the middle of that range and a commensurate uncertainty value until further information is gathered.

Uncertainty in the SHFG

The uncertainty associated with the SHFG has been examined in significant detail, in Ref. 4. Uncertainty associated with material properties (heat capacity, conductivity, & emissivity), dimensions, losses (convection and conduction to the insulation layer), time lags and thermocouple readings and noise are all considered. Altogether, 17 different sources of uncertainty were considered. Estimates of the expected uncertainty for each variable are included and the results are combined together using a root-of-sum-of-squares approach (similar to Eq. 4) to yield an estimate of the overall uncertainty. The spreadsheet macro automatically calculates the individual uncertainty components as well as the overall total. It should be noted that here we have NOT included the "missing physics" uncertainty described in Ref. 4. This primarily affected the initial transient (immediately after propellant burning began), but otherwise seemed to yield an inordinate amount of "noise" to the uncertainty bounds (caused by amplified numerical differentiation) that was not present in the baseline flux.

As described in the modeling section, we expect the SHFG to be subject to considerable uncertainty associated with multi-dimensional heat transfer, particularly for the short time scales (a few minutes) of the solid

propellant tests. The estimated bounding envelopes derived from the modeling effort described previously were combined with the output of the SHFG analysis spreadsheet macro. Because these multidimensional effects in these cases always result in an under-prediction, the associated error is a one-sided systematic or bias error. Hence instead of being combined in a root-of-sum-of-squares fashion these are instead added directly to the upper and lower bounds obtained from the spreadsheet macro.

HEAT FLUX DERIVED FROM EXPERIMENTS

Data for all the DFTs and SHFGs (7 of each type of sensor) from all of the four tests were processed to obtain derived incident heat flux resulting in 56 full data sets. For clarity we will first highlight results from a single test and location in order to compare uncertainty behavior between the two devices. Figure 10 shows the incident heat flux from Experimental Test Matrix 1 (50.8 cm diameter propellant charge) at the lowest location on the heat flux gauge tower (25.4 cm above charge), along with the associated uncertainty bands described previously. Results are obtained from both the SHFG and the DFT. Comparing the two sets of results highlights some interesting observations. First, as we expected based on the multi-dimensional heat transfer effects, the analyzed DFT response gives a significantly higher incident flux level than the SHFG (~45 vs. ~34 kW/m^2). Second, the SHFG appears to react slightly more quickly than the DFT; this may be expected given the much thinner sensor plate thickness. Third, the error bounds for the DFT and SHFG (uncorrected) have similar magnitudes (on the order of ±10% variation during the time period from ~50 sec to 130 sec). The correction for multidimensional heat transfer on the SHFG dramatically increases the upper and lower bound range. If this correction is made, the two devices do appear to give coincident results; if not, the difference between the two devices cannot be adequately explained from just random uncertainties.

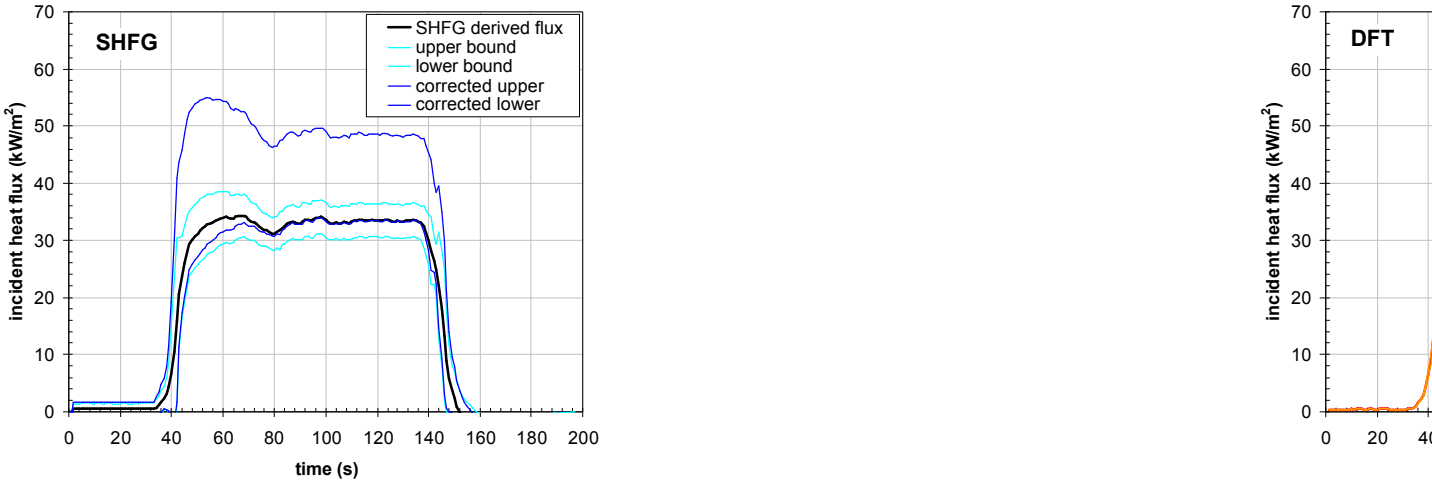

Fig. 10: Derived incident heat flux and uncertainty bands for Test Matrix 1 at lowest flux gauge tower location (25.4 cm). Left: SHFG response with upper and lower uncertainty bounds with and without the multi-dimensional heat transfer correction. Right: DFT response with uncertainty band.

Importance factors (F_ϕ, from Eq. 5) were calculated for the 17 uncertain parameters considered in the SHFG analysis and for the 7 parameters for the DFT analysis. The DFT showed very clearly that the emissivity was the dominant factor accounting for 80% of the total uncertainty. The second and third highest contributors were the heat capacity of the Inconel® with ~16% and the Inconel® plate thickness with ~3%. These stayed relatively constant through much of the times of interest (40 to 140 sec). In contrast, the SHFG analysis showed that various factors were important at various times. The top three contributors to uncertainty were the sensor plate thickness, the thermocouple time lag, and the assumption of 1-D conduction in the insulation (recall that multi-dimensional heat transfer in the sensor plate was NOT considered by the spreadsheet macro).

The incident heat flux from the four experiments and seven sensor locations were obtained from analysis. Figure 11 shows the radiant flux derived from the SHFG (left hand side) and the DFT (right hand side). Here for clarity, we have NOT included the uncertainty bounds. If they were to have been included they would be proportionally the same as shown in Fig. 10 (e.g. ~10% for the DFTs etc.). Note that similar to the results in Fig. 10, the response derived from the DFTs exceed significantly that derived from the SHFGs.

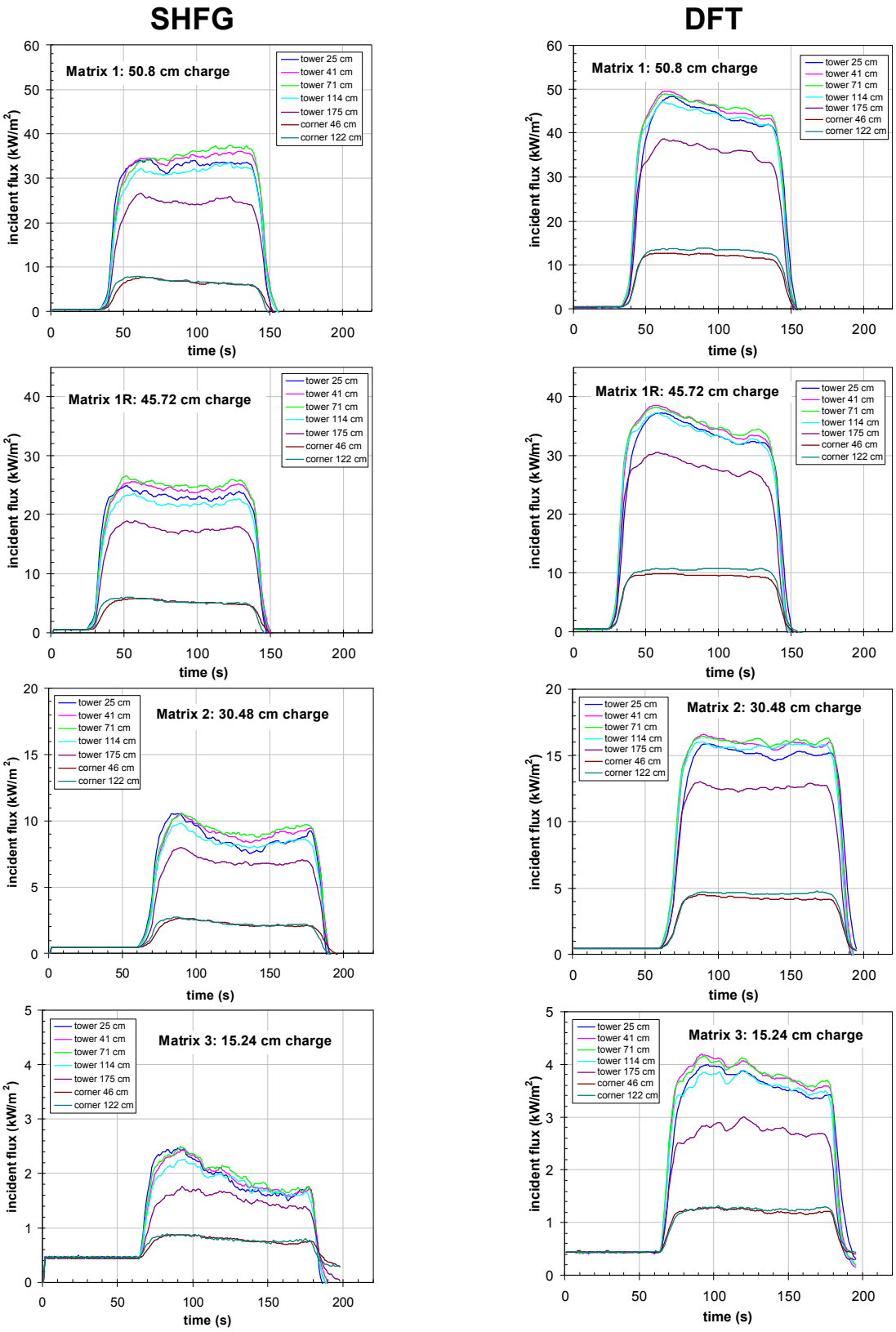

Fig. 11: Derived incident heat flux from solid propellant Test Matrices 1, 1R, 2, and 3 using SHFG (left) or DFT (right). Uncertainty bounds are not shown here for clarity.

COMPARISON WITH SCHMIDT-BOELTER GAUGES

In addition to the array of DFTs and SHFGs, the propellant burn tests also were monitored by Schmidt-Boelter (SB) heat flux gauges mounted in the corners of the test chamber (see Fig. 9). Both narrow angle and hemispherical SB gauges were used. The narrow angle gauges focused on the propellant flame itself so are less useful for comparison with the DFTs and SHFGs. But the hemispherical SB gauges should compare well, particularly since their distance from the plume is nearly the same as the corner-mounted DFTs and SHFGs.

Figure 12 shows a comparison of the incident heat flux derived from the three types of gauges mounted in the corner of the facility for the four propellant burns of interest (only nominal values are shown—for clarity, we have not included the uncertainty ranges here. Two gauges of each type (SB, DFT, SHFG) reported, except for Matrix 1 in which one of the SB gauges failed and the other appeared to read somewhat anomalously early in the test. The data appear to show a significant level of agreement between the DFTs and the commercial SB gauges, while as we have come accustomed to expect the SHFGs appear to read low; probably because of the multidimensional heat losses on the sensor plate. The results from Matrix 3 appear to have the least agreement, however the flux levels on that test were low enough that noise begins to play a larger role (e.g. note the bit toggling present in the SB gauge record).

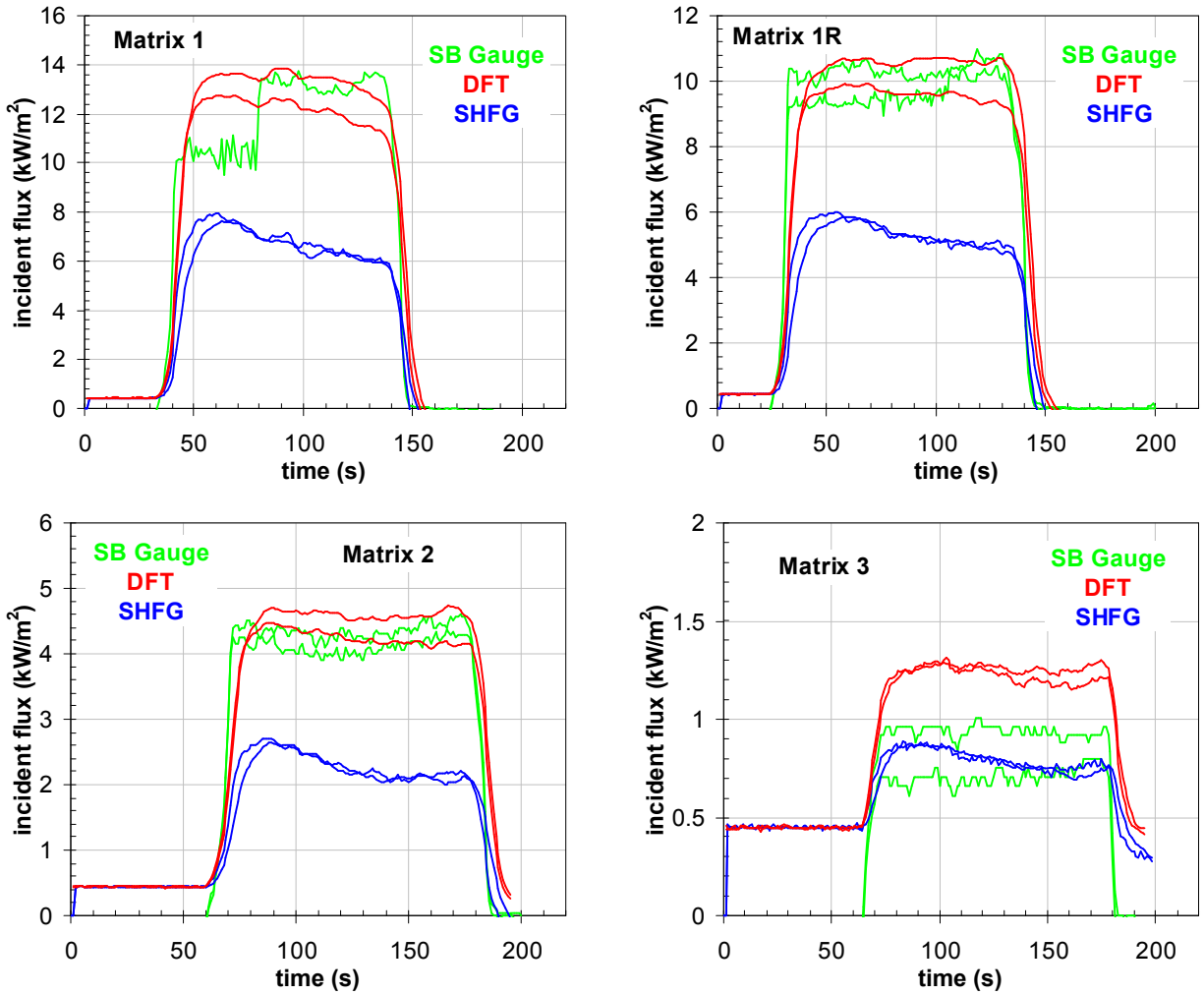

Fig. 12: Comparison of incident flux derived from propellant burn data using three types of heat flux sensors. All were mounted in the corners of the facility and are nominally the same distance from the propellant.

HEAT FLUX SCALING

One item of interest for safety analysis and other purposes is the scaling of radiant energy flux with the size of the propellant burning. It is of interest whether one can simply use the overall burning rate of propellant as a multiplicative scaling factor or whether the effects are non-linear. As a check, we took the DFT-derived heat fluxes from all four tests and normalized them by dividing by the burning area of the propellant (i.e. $\pi d^2/4$). The left side of Figure 13 shows the effect. Note that even though the burning area changes over a range of more than an order of magnitude among the four tests, there is very little effect once the flux is normalized.

Taking this one step further, we can estimate the fraction of the energy of combustion which is delivered as radiation to the surroundings. This was done by integrating the heat flux which arrived at a cylinder surrounding the propellant fire. Here we used the cylinder defined by the heat flux gauge locations on the tower supporting the heat flux gauges (located at a radius of 1.54 m, see Fig. 9). The length of this cylinder is 1.5 m; it extends from the lower gauge location (25 cm) to the uppermost gauge location (175 cm). The cylinder was divided into rings over which the heat flux was considered constant. By summing the contributions of all the rings the integrated heat flux was determined. This quantity was then divided by the product of the mass burning rate of the propellant (= linear burning rate x burning area x propellant density) and the heat of combustion (in excess air, this propellant has a heat of combustion of 12.47 kJ/g assuming all the aluminum burns to completion as determined by the Cheetah thermochemical equilibrium code[13]). The result is a fraction of the energy of combustion which is radiated outward. The right hand side of Fig. 13 shows this fraction as determined from the SHFG and DFT data. Note that the DFT0-derived results seem to indicate a constant fraction of about 15%, whereas the DFT data may show a trend which changes with size. However, the large uncertainty ranges for the SHFG permit a constant value as well. It should also be remembered that there will be more than the 15% radiation—there will be additional radiation above and below the 1.5 m cylinder. We will not attempt to estimate this additional contribution here.

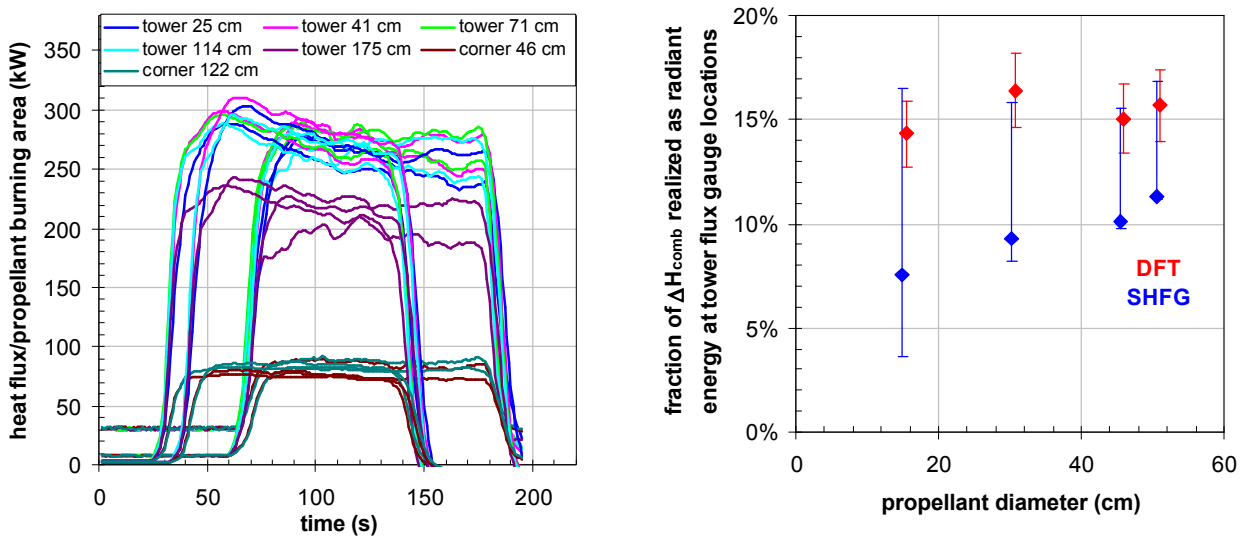

Fig. 13: Left: incident radiant heat flux normalized by the burning area of the propellant for four tests. Right: Fraction of combustion energy emitted as radiation as captured by tower heat flux gauges.

VULCAN MODEL RESULTS

Computational fluid dynamics/combustion codes are being developed as tools to predict behavior of solid propellant burning under ambient air conditions including sub-models for particle combustion and radiation.[14,15] Previously simulations were made of the upward cylindrical burns and predictions of radiation heat transfer in the locations of the heat flux gauges were made. However in the previous report (c.f. Ref. 14), anomalous behavior was observed in the spatial distribution of heat flux. It was discovered later that the ray-tracing algorithm used for radiation heat transfer predictions at the gauges had not sufficiently resolved the radiation environment—an insufficient number of rays passed through the gauge locations to get reasonable statistics. This has recently been remedied.

Figure 14 shows VULCAN CFD code predictions of the incident radiation flux at the tower gauge locations for Test Matrices 1, 2, and 3. We also show the results derived from the DFT and SHFG experiments. The VULCAN simulations appear to capture the trends in terms of variations with height. However, in an absolute sense, the VULCAN results tend toward the lower end of the ranges, and largely falling below the range of the DFT-derived results.

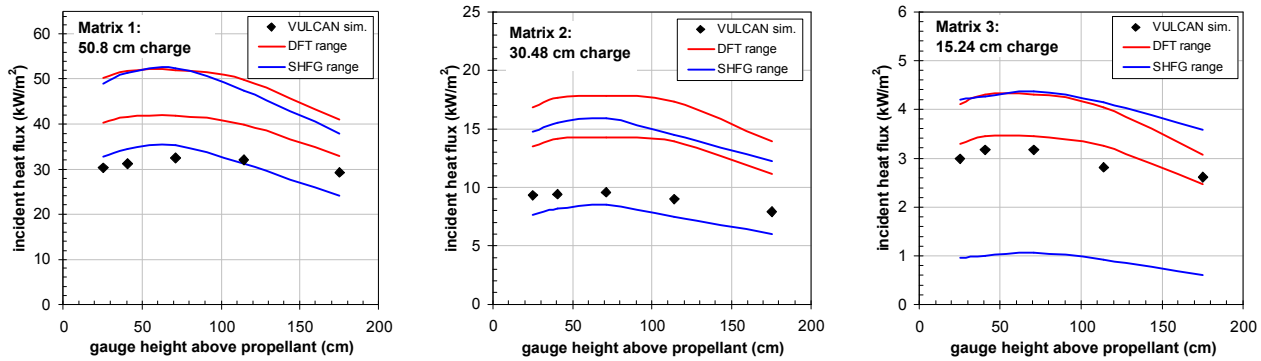

Fig. 14: Comparison of Vulcan CFD simulations with DFT and SHFG derived incident flux measurements for Test Matrices 1, 2, and 3. DFT and SHFG results are presented as uncertainty ranges between lines. The SHFG range includes the multi-dimensional correction term. The Vulcan simulations are represented as points.

SUMMARY AND CONCLUSIONS

Here we have presented an analysis technique which used modeling and simulation to address uncertainties present in experimental heat flux measurements. Two types of specialty gauges (SHFGs and DFTs) were considered using detailed finite element models subjected to known boundary conditions. Errors associated with the gauges were quantified. Of particular note, it appears that the SHFG suffers from a significant amount of error associated with multidimensional heat conduction within the sensor plate. Uncertainty bounds for the SHFG were enlarged to account for this error.

Data from four propellant burns were analyzed to yield incident heat flux together with the associated uncertainty bounds. The DFT-derived heat fluxes typically read noticeably higher than that derived from SHFGs. Comparison with commercial Schmitt-Boelter gauges indicated consistent agreement between the DFTs and the SB gauges. SHFG results were at noticeably lower levels. Comparison was also made with CFD simulations using the VULCAN code. VULCAN reproduced qualitatively the trends of heat flux versus height, however the absolute magnitude appears to be lower than that obtained from the experiments. At this point, the apparent uncertainty in the CFD modeling is large—the simulations appear to be about 50% lower than our best estimates based on the DFTs.

Analysis of the experiments indicated that the fraction of the combustion energy manifest as radiation is nearly constant with size of burning propellant. Based on the 1.5 m high arrays of heat flux gauges deployed, the radiation fraction is at least 15%; energy radiated above and below these was not considered.

FUTURE WORK

Based on the results of this study, we believe a number of improvements can be made to both the DFT and the SHFG. The DFT would benefit from having a better control on surface emissivity. We suggest that painting with a well-characterized, high-temperature coating such as Pyromark® would significantly reduce the uncertainty. Although the effect was minimal for the short time tests we considered here, there is also potential for significant heat losses from bolt conduction over the long term. We suggest thermally isolating the bolts from the sensor plates.

Improvements can also be made to the SHFG. Clearly, lateral heat transfer on the sensor plate must be accounted for. Perhaps this could be done by including an additional thermocouple mounted near the edge of the exposed portion of the sensor plate. Using the difference in temperature between the two locations may allow the sensor to mimic the behavior of Gardon heat flux gauges which assume a parabolic profile across a thin membrane.

We also plan to explore reasons for the under-prediction of the CFD simulations for heat flux and thereby improve our propellant fire modeling capability. At the present, we can carry the model forward with the understanding that it will under-predict in scenarios similar to these tested.

ACKNOWLEDGEMENTS

This work was supported by Sandia National Laboratories under the Campaign 6 and Weapons Systems Qualification programs. Propellant material was obtained from Aerojet Corporation.

We recognize the outstanding contributions by a large number of individuals who designed and built the heat flux sensors, contributed to the operation of experiments, and helped to make this work possible.

REFERENCES

[1] Darwin, R. L. "U.S.S. Stark Battle Damage and Fire Protection Lessons Learned," *Journal of Naval Engineering*, Vol. 31, No. 2, December 1988.
[2] Erikson, W. W. and Gill, W., "Analytic Model for Propellant Fire Heat Transfer with Deposition," *JANNAF 40th CS, 28th APS, 22nd PSHS, and 4th MSS Joint Meeting*, Charleston, SC, June 2005.
[3] Erikson, W. W. and Gill, W., "A Multi-dimensional Heat Transfer Model for Objects Subjected to Ambient Air Solid Propellant Fires," *JANNAF 55th JPM, 42nd CS, 30th APS, 30th EPTS, 24th PSHS, 12th SPIRITS User Group Joint Meeting*, Boston, MA, May 2008.
[4] Blanchat, T. K., Humphries, L. L., and Gill, W. "Sandia Heat Flux Gauge Thermal Response and Uncertainty Models," Sandia National Laboratories Report, SAND2000-1111, May 2000.
[5] Keltner, N., "Using Directional Flame Thermometers – DFTs," F.I.R.E.S., Inc. Report dated 4/07/2006.
[6] Keltner, N., personal communication, electronic mail "RE DFT design" to V. Figueroa et al. dated 7/3/2008.
[7] Beck, J. V., "User's Manual for IHCP1D: Program for Calculating Surface Flux from Transient Temperatures inside Solids," Beck Engineering Consultants, Co. Okemos, MI, 1999.
[8] Figueroa, V., Gill, W., Erikson, W. W., Reinhart, L. E. and Dowler, W. L. "Design and Implementation of JPL-NASA Propellant Fire Test Series," *JANNAF 55th JPM, 42nd CS, 30th APS, 30th EPTS, 24th PSHS, 12th SPIRITS User Group Joint Meeting*, Boston, MA, May 2008.
[9] Gill, W., Erikson, W. W. and Nicolette, V. F. "Heat Flux from Ambient Air Solid Propellant Fire Plumes," *JANNAF 55th JPM, 42nd CS, 30th APS, 30th EPTS, 24th PSHS, 12th SPIRITS User Group Joint Meeting*, Boston, MA, May 2008.
[10] Reinhart, L. E., Bowman Jr., R. C., Li, H., Kulleck, J. G., and Dowler, W. L. "Overview of NASA-JPL Ambient Air Solid Propellant Fire Test Program, Including Analyses Completed at JPL," *JANNAF 55th JPM, 42nd CS, 30th APS, 30th EPTS, 24th PSHS, 12th SPIRITS User Group Joint Meeting*, Boston, MA, May 2008.
[11] Woodbury, K. A., Keltner, N., Noravian, H., and Reinhart, L. E., "Characterization of a Rod Calorimeter and Validation of Experimental Results from a Solid Propellant Burn," *JANNAF 55th JPM, 42nd CS, 30th APS, 30th EPTS, 24th PSHS, 12th SPIRITS User Group Joint Meeting*, Boston, MA, May 2008.
[12] Sivathanu, Y., Lim, J., Reinhart, L. E., Bowman, R., Gill, W., and Figueroa, V. "Structure of Aluminized Propellant Plumes Obtained Using Multi-Angular Infrared Emission Spectroscopy," *JANNAF 55th JPM, 42nd CS, 30th APS, 30th EPTS, 24th PSHS, 12th SPIRITS User Group Joint Meeting*, Boston, MA, May 2008.
[13] Fried, L. E. et al., *Cheetah 5.0 User's Manual,* Lawrence Livermore National Laboratory, December, 2004.
[14] Nicolette, V. F. and Hewson, J. C., "Modeling the Thermal Environment from Ambient Atmosphere Solid Propellant Fires," *JANNAF 55th JPM, 42nd CS, 30th APS, 30th EPTS, 24th PSHS, 12th SPIRITS User Group Joint Meeting*, Boston, MA, May 2008.
[15] Hewson, J. C. and Nicolette, V. F., "Predicting Aluminum Droplet Burning Rates with Varying Oxidizers," *JANNAF 55th JPM, 42nd CS, 30th APS, 30th EPTS, 24th PSHS, 12th SPIRITS User Group Joint Meeting*, Boston, MA, May 2008.